High-Pressure XAFS Measurements of the Coordination Environments of Fe^{2+} and Fe^{3+} in Basaltic Glasses

Keisuke Ozawa[1], Kei Hirose[1,2], and Yoshio Takahashi[1,3]

[1]Department of Earth and Planetary Science, The University of Tokyo, Tokyo, Japan

[2]Earth-Life Science Institute, Tokyo Institute of Technology, Tokyo, Japan

[3]Institute of Materials Structure Science, High-Energy Accelerator Research Organization, Tsukuba, Ibaraki, Japan

Key Points

- We examined high-pressure coordination environments around Fe^{2+} and Fe^{3+} in basaltic glasses by X-ray absorption spectroscopy to 83 GPa.
- XANES and EXAFS analyses indicate that the coordination numbers of Fe^{2+} and Fe^{3+} increases with increasing pressure from 1 bar to ~15 GPa.
- Compression behaviors of the Fe-O bond lengths support the disproportionation of Fe^{2+} into Fe^{3+} and Fe^{0} in a deep magma ocean.

Abstract We investigated pressure-induced changes in the coordination environments of Fe^{2+} and Fe^{3+} in basaltic glasses based on the Fe K-edge X-ray absorption fine structure (XAFS) analyses for both XANES and EXAFS regions. Upon compression from 1 bar to ~15 GPa, the Fe^{2+}-O bond length remained similar, suggesting that the average coordination number of Fe^{2+} increased from ~5 to 6. On the other hand, the Fe^{3+}-O bond

was remarkably elongated, which indicates that Fe^{3+} changed from 4-fold to 6-fold coordination. Above 15 GPa, both Fe^{2+}-O and Fe^{3+}-O bond lengths decreased smoothly, suggesting minor changes in their coordination numbers. The data also showed that both Fe^{2+} and Fe^{3+} remained in the high-spin state up to 83 GPa and 60 GPa, respectively, in the basaltic glasses. These compression behaviors of the Fe^{2+}-O and Fe^{3+}-O bonds support that Fe^{2+} disproportionates into Fe^{3+} and metal Fe in a deep magma ocean.

Plain Language Summary The coordination environments around Fe^{2+} and Fe^{3+} in silicates are of great importance for their partial molar volumes, spin states, and partitioning. The local structures around Fe in silicate glasses were intensively studied at 1 bar by XAFS analyses, but their pressure-induced changes have not been examined. Here we conducted the XAFS measurements of Fe^{2+} in a reduced basaltic glass to 83 GPa and Fe^{3+} in an oxidized glass to 60 GPa. While the Fe-O bond is shortened by a simple compression effect, it is elongated due to an increase in the coordination number. The observed changes in the bond length showed that Fe^{2+} was ~5-fold coordinated at 1 bar and became 6-fold with compression to ~15 GPa. On the other hand, the coordination number of Fe^{3+} increased from 4 at ambient pressure to 6 at ~15 GPa. Both were 6-fold coordinated above 15 GPa. These bond lengths also suggest that both Fe^{2+} and Fe^{3+} remained high spin in our measurements. The difference between the Fe^{2+}-O and Fe^{3+}-O bond lengths support a previously-proposed negative volume change upon the disproportionation reaction of Fe^{2+} into Fe^{3+} and Fe^{0} above 10 GPa, which enhances such disproportionation in a deep magma ocean.

1. Introduction

Iron is the most abundant transition metal and exhibits multiple oxidation states in the Earth's mantle. The coordination environments and bond lengths of Fe^{2+}-O and Fe^{3+}-O in silicates change with increasing pressure. The spin states of Fe^{2+} and Fe^{3+} could also change not only in solid phases (Badro et al., 2003; Zhang & Oganov, 2006) but also in melts and glasses under high pressure (Nomura et al., 2011; Gu et al., 2012; Karki & Ghosh, 2018). The changes in the Fe^{2+}-O and Fe^{3+}-O bond lengths will tell their possible spin crossovers under lower-mantle pressures. It has been also suggested that Fe^{2+} disproportionates into Fe^{3+} and metal Fe in a deep magma ocean, depending on the partial molar volumes of FeO and $FeO_{1.5}$ and their compressibilities (O'Neill et al., 2006; Zhang et al., 2017; Armstrong et al., 2019). However, direct measurements of these properties are limited to 1 atm (Lange & Carmichael, 1987; Kress & Carmichael, 1991). They are dependent on the coordination environment of Fe ions, in particular their coordination number and the structure of silicate melts, both of which will change under high pressure (Sanloup et al., 2013a). However, the change in the coordination environment of iron in silicate melt has been experimentally investigated only up to 7.5 GPa by X-ray diffraction measurements (Sanloup et al., 2013b).

The XAFS spectrum is sensitive to the local structure of a specific element of interest including the bond length. It is therefore a useful tool for elucidating changes in the coordination environments and spin states of Fe^{2+} and Fe^{3+} under high pressure. However, the XAFS study of Fe^{2+} and Fe^{3+} in a silicate glass has been difficult at high pressures because diamond anvils absorb X-rays to a large extent at the Fe absorption edge energy (~7.1 keV), while the ambient-pressure XAFS measurements of Fe in silicate glasses have been intensively reported (Farges et al., 2004; Wilke et al., 2007).

70 Here we conducted the XAFS measurements of Fe^{2+} and Fe^{3+} in reduced and oxidized
71 basaltic glasses, respectively, at high pressures in the fluorescence yield mode (Ozawa et
72 al., 2021). The analyses of X-ray absorption near edge structure (XANES) including pre-
73 edge structure and extended X-ray absorption fine structure (EXAFS) demonstrate
74 changes in the Fe^{2+}-O and Fe^{3+}-O bond lengths with increasing pressure up to 83 GPa and
75 60 GPa, respectively, indicating their coordination environment and spin state under
76 pressure. Based on these results, we discuss the spin crossover of Fe^{2+} and Fe^{3+} in basaltic
77 glasses and the disproportionation of Fe^{2+} into Fe^{3+} and Fe^{0} in a deep magma ocean.

78 ## 2. Results

79 We collected nine and eight XAFS (both XANES and EXAFS) spectra of reduced and
80 oxidized basaltic glasses with increasing pressure from 1 bar to 83.2 GPa and to 60.0 GPa,
81 respectively (see Experimental Methods in the Supporting Information). The Fe K-edge
82 XANES spectrum comprises three separate features relating to transitions of electrons to
83 different excited states: pre-edge (1s→3d), threshold energy (1s→4s), and white line
84 (1s→4p) (Waychunas et al., 1983) (Figure 1).

85 ### 2.1. Pre-edge Structure

86 The pre-edge features were extracted from the normalized XANES spectra to emphasize
87 their characteristics (Figure 1). The calculated centroid position and integrated intensity
88 for the pre-edge absorbance are given for all the spectra in Table S2. The centroid energy
89 and intensity of the pre-edge absorbance at the Fe K-edge are sensitive to the oxidation
90 state and coordination environment of iron atoms in a sample, respectively (Figure 2).

The centroid position of the reduced basalt glass is 7111.92 eV at ambient pressure (Figure 2), indicating that almost all iron was Fe^{2+} in our reduced glass according to Wilke et al. (2005). Its pre-edge intensity observed at 1 bar is consistent with those for reduced basaltic glasses (Wilke et al., 2005) and reduced silicate melts (Alderman et al., 2017), which shows that the coordination number of Fe^{2+} is close to five. As pressure increased, the pre-edge intensity became closer to those of minerals with octahedrally coordinated ferrous iron (Figure 2). This observation suggests that the average coordination number of Fe^{2+} in our reduced glass increased with compression from ~5 at ambient pressure to 6 above 15 GPa.

On the other hand, the centroid position of the oxidized glass is 7113.40 eV at 1 bar (Figure 2), showing $Fe^{2+}/\Sigma Fe = 0.21$, which is consistent with the ratio expected for the condition where this glass was synthesized. Its pre-edge intensity suggests that Fe^{3+} is almost 4-fold at 1 bar. While Wilke et al. (2005) interpreted that Fe^{3+} in their oxidized glass was 5-fold, the pre-edge intensity itself is similar between this study and their measurements, and the discrepancy is attributed to the variation in the pre-edge intensity of reference minerals for tetrahedrally-coordinated Fe^{3+} (Boubnov et al., 2015). The change in the pre-edge intensity with increasing pressure also indicates that the average coordination number of Fe^{3+} increased upon compression from almost 4 at 1 bar to 6 above 15 GPa (Figure 2).

2.2. Absorption Edge Structure

The information on the valence state of Fe ion and the Fe-O bond length are included not only in the pre-edge feature but also in the absorption edge structure, in particular (i) the peak energy of the white line and (ii) the threshold energy, which is a structure around

the maximum of $d\mu_N/dE$ (μ_N, normalized absorbance; E, energy) (Figure 1 and Table S2). It is known that both the white line peak energy and the threshold energy are higher for Fe^{3+} than for Fe^{2+}.

In the case of the reduced glass, the while line peak energy significantly increased with increasing pressure above 15 GPa (Figure 3a). Indeed, the increase in the peak energy is well correlated to the shortening of the average Fe^{2+}-O bond length (see the next section) (Figure S1). Previously Waychunas et al. (1983) reported similar observations in minerals. In contrast, the threshold energy changed little with increasing pressure (Figure 3c). While the first derivative spectrum at ambient pressure had a double-peaked shape (Berry et al., 2003), it gradually became single-peak as pressure increased. The effect of silicate glass composition may be important for the threshold energy; a reduced W-doped basaltic glass exhibited a distinct value (Ozawa et al., 2021) (Figure S2). It contrasts the fact that the compositional effect on the white line peak energy is quite small.

Our data on the oxidized glass demonstrate a negative correlation between the Fe^{3+}-O bond length and the peak position of the white line for Fe^{3+}, similar to the case of Fe^{2+} (Figure S1). The white line peak energy certainly decreased with increasing pressure from 1 bar to ~15 GPa and then increased at higher pressures (Figure 3b). It should be attributed to the increase and subsequent decrease in the Fe^{3+}-O bond length in our oxidized glass (see the next section). The first-derivative spectrum at 1 bar given in Figure 3d is similar to that of an Fe^{3+}-rich silicate glass in Berry et al. (2003). The correlation between the e^{3+}-O bond length and the threshold energy is not clear (Figure S2).

2.3. EXAFS Spectra

All of the present XAFS measurements include the EXAFS spectra that provide the Fe-O bond length quantitatively. The extracted k^3-weighted oscillations are shown in Figure S3. Considering that all Fe was Fe^{2+} in the reduced glass, we determined the Fe^{2+}-O bond length at each pressure from the EXAFS analyses (Figure 4 and Table S2).

We obtained the Fe^{2+}-O bond length r_{Fe2+-O} = 1.98 ± 0.02 Å at 1 bar for the reduced basaltic glass (Figure 4a). The r_{Fe2+-O} remained constant within errors up to 15.1 GPa, in which the bond length elongation because of an increase in the coordination number was compensated by shortening due to a simple compression effect. At higher pressures, the average Fe^{2+}-O bond length decreased continuously with increasing pressure up to 83.2 GPa. In this pressure range, the effect of the coordination number increase may be minor. The shortening per a given pressure increase above 15 GPa is found to be greater than that of the Si-O (Prescher et al., 2017) and Ge-O bonds (Hong et al., 2014) (Figure 4b).

The Fe^{3+}-O bond length in our oxidized glass was also determined at each pressure from the EXAFS analyses. At 1 bar, r_{Fe3+-O} is found to be 1.87 ± 0.02 Å (Figure 4a), consistent with the interatomic distance between four-fold Fe^{3+} and O in a peralkaline rhyolitic glass at ambient pressure (Giuli et al., 2012). The Fe^{3+}-O bond length increased with increasing pressure up to 16.2 GPa unlike the case of Fe^{2+}, indicating that the effect of the coordination number increase exceeded the simple bond length shortening by compression. With further compression from 16.2 GPa to 60.0 GPa, the Fe^{3+}- O bond length decreased constantly as for Fe^{2+}.

As described above, we found negative correlations between the Fe^{2+}-O/Fe^{3+}-O bond lengths and the white line peak energy (Figure S1), which indicates that the coordination number has little influence on the peak position of the white line. On the other hand, the

159 threshold energy also shows negative correlation with the Fe^{2+}-O bond length, but does
160 not have a clear correlation with the Fe^{3+}-O bond length (Figure S2). The white line peak
161 position in the XANES spectra can be a good indicator of the Fe^{2+}-O/Fe^{3+}-O bond lengths
162 in silicate melts and glasses when high-quality EXAFS data are not available.

163 ## 3. Discussion

164 ### 3.1. Compression Behaviors of Fe^{2+} and Fe^{3+} in Basaltic Glasses

165 The present pre-edge and EXAFS analyses showed that Fe^{3+} is almost 4-fold coordinated
166 in our basaltic glass sample at 1 bar, while Fe^{2+} is ~5-fold coordinated (Figure 2). The 4-
167 fold Fe^{3+} is considered to be a network former, polymerizing silicate melt/glass structures
168 and being accompanied with a charge compensator ion like Na^{+} and Ca^{2+}. In contrast, the
169 ~5-fold Fe^{2+} is a network modifier or plays an intermediate role (Alderman et al., 2017).

170 Below ~15 GPa, while the Fe^{2+}-O bond length remained similar, the Fe^{3+}-O bond was
171 elongated remarkably with compression (Figure 4a). Such difference is likely due to the
172 difference in their coordination number at 1 bar; the large increase in the Fe^{3+}-O bond
173 length below 15 GPa is attributed to an increase in the coordination number of ferric iron
174 from four to six, whereas the approximately uniform Fe^{2+}-O bond length is likely a
175 consequence of a small increase in its coordination number from about five to six. At the
176 higher pressure range, both the Fe^{2+}-O and Fe^{3+}-O bond lengths decreased similarly with
177 increasing pressure (Figure 4a), in which the effect of an increase in the coordination
178 number is likely to be minimal.

179 We compare the pressure-induced changes in the Fe^{2+}-O and Fe^{3+}-O bond lengths
180 observed in this study with those of Mg^{2+}-O (Ghosh & Karki, 2020), Ca^{2+}-O and Al^{3+}-O

(Ghosh & Karki, 2018), Si^{4+}-O (Prescher et al., 2017), Ge^{4+}-O (Hong et al., 2014), and W^{6+}-O (Ozawa et al., 2021) previously reported in silicate/germanate melt and glasses (Figure 4a, b). For both Mg^{2+} and Ca^{2+}, the bond lengths are almost constant from ambient pressure to 15 GPa, similar to the case of Fe^{2+}-O, indicating that the bond elongation by coordination number increase and the bond shortening by a simple compression effect are balanced. In contrast, the Al^{3+}-O bond length increases with pressure to 15 GPa as for Fe^{3+}, which indicates the role of Fe^{3+} in silicate glass structures is similar to that of Al^{3+} at such low pressure range. At higher pressures (>15 GPa for Ca^{2+}, Mg^{2+}, Al^{3+}, Fe^{2+}, and Fe^{3+}, >~20 GPa for Ge^{4+}, and >~30 GPa for Si^{4+} and W^{6+}), the bond lengths then decrease with compression (Figure 4a, b). The Fe^{2+}-O and Fe^{3+}-O bond lengths became shorter by -0.0015 Å/GPa and -0.0017 Å/GPa, respectively. They are equivalent to -0.0017 Å/GPa for Mg^{2+}-O in $(Mg,Fe)SiO_3$ melt at 3000 K (Ghosh & Karki, 2020) and -0.0024 Å/GPa for Ca^{2+}-O in $CaAl_2Si_2O_8$ glass (Ghosh & Karki, 2018). The similarity to the Mg^{2+}-O and Ca^{2+}-O bonds suggests that not only Fe^{2+} but also Fe^{3+} act as network modifiers under high pressures where they are predominantly six-fold coordinated. In contrast, for high field strength elements (with large valence/ionic-radius ratios), Si^{4+}-O in SiO_2 glass (-0.0006 Å/GPa), Ge^{4+}-O in GeO_2 glass (-0.0004 Å/GPa), W^{6+}-O in basaltic glass (-0.0001 Å/GPa), and Al^{3+}-O in $CaAl_2Si_2O_8$ glass (-0.0005 Å/GPa) exhibit more gradual changes (Prescher et al., 2017; Ozawa et al., 2021; Ghosh and Karki, 2018). These Si^{4+}, Ge^{4+}, W^{6+}, and Al^{3+} are the network forming cations with six-fold coordination at >~30 GPa. The gradual decrease in these bond lengths may be a result of the volume reduction by enhanced distortion of coordinated octahedra instead of isostructural compression (Spiekermann et al., 2019).

3.2. Spin Crossover of Iron in Silicate Glasses

Previous studies examined possible spin crossovers of ferrous and ferric iron in silicate glasses under high pressures based on X-ray emission spectroscopy (XES) and Mössbauer spectroscopy (Nomura et al., 2011; Gu et al., 2012; Murakami et al., 2014; Mao et al., 2014; Prescher et al., 2014; Dorfman et al., 2016; Solomatova et al., 2017). The Fe^{2+}-O and Fe^{3+}-O bond lengths obtained by XAFS measurements also show the spin state of ferrous and ferric iron at high pressures.

In Figure 4c, we compare the Fe^{2+}-O and Fe^{3+}-O bond lengths in our glass samples determined by the EXAFS analyses with those in Fe-bearing $MgSiO_3$ melt at 3000 K obtained by first principles molecular dynamics simulations (Ghosh & Karki, 2020). Although the bond lengths in the latter are longer partly because of thermal expansion, they exhibit similar pressure effects. The behavior of the Fe^{2+}-O bond length below 15 GPa is an exception; while it increased rapidly in the Fe-bearing $MgSiO_3$ melt, it changed little in our reduced glass. Such difference can be attributed to the difference in the coordination number of ferrous iron at ambient pressure; it was shown to be less than four in silicate (basaltic) melts by previous first principles simulations (Bajgain et al., 2015; Solomatova & Caracas, 2019; Ghosh & Karki, 2020), whereas it has been reported to be about five in glasses and melts by experimental studies including the present one (Alderman et al., 2017).

Upon compression from 15 to 83 GPa, the Fe^{2+}-O bond length in our basaltic glass decreased smoothly by ~0.1 Å (Figure 4c). Such shortening is similar to that calculated for the high-spin Fe^{2+} in $Mg_{0.75}Fe_{0.25}SiO_3$ melt (Ghosh & Karki, 2020). They also calculated for the low-spin Fe^{2+}, demonstrating much shorter bond lengths by ~0.2 Å

227 above 15 GPa (such difference is consistent with the difference in the ionic radius
228 between six-fold high-spin and low-spin ferrous iron at 1 bar). The supposed low-spin
229 Fe^{2+}-O bond length in a basaltic glass based on the calculations by Ghosh & Karki (2020)
230 is substantially shorter than that of Fe^{2+}-O observed in this study.

231 Previous XES measurements of $Mg_{0.95}Fe_{0.05}SiO_3$ glass (Nomura et al., 2011) and
232 $Mg_{0.8}Fe_{0.2}SiO_3$ and $Mg_{0.75}Fe_{0.20}Al_{0.05}SiO_3$ glasses (Gu et al., 2012) demonstrated a
233 complete spin crossover of ferrous iron at 77 GPa and a partial loss of spin moment at
234 >93 GPa, respectively. In addition, the Mössbauer measurements by Murakami et al.
235 (2014) suggested a transition of Fe^{2+} to an intermediate-spin state in $(Mg_{0.8}Fe_{0.2})SiO_3$
236 glass. In contrast, Mao et al. (2014) analyzed the XES spectra taking the broadening effect
237 into consideration and argued that all Fe remains in the high-spin state in an (Al, Fe)-
238 bearing silicate glass up to 126 GPa. The Mössbauer study by Solomatova et al. (2017)
239 argued that ferrous iron remains high-spin to ~100 GPa in a basaltic glass. The present
240 data supports high-spin Fe^{2+} in basaltic glasses up to 83 GPa (Figure 4c). The apparent
241 discrepancies among these studies may be attributed to the differences in glass
242 composition.

243 The compression behavior of the Fe^{3+}-O bond length in our oxidized glass is similar to
244 that theoretically calculated for the high-spin Fe^{3+} in $Mg_{0.875}Fe^{3+}_{0.25}Si_{0.875}O_3$ melt (Ghosh
245 & Karki, 2020) (Figure 4c). Such similarity supports that Fe^{3+} remains high spin, at least
246 to 60 GPa. The XES and Mössbauer measurements on $Fe_3Al_2Si_3O_{12}$ almandine glass by
247 Dorfman et al. (2016) argued for the high-spin to low-spin crossover of Fe^{3+} between
248 ambient pressure and 30 GPa. Such discrepancy may be also due to the difference in glass
249 sample composition. Alternatively it is also possible that the Mössbauer observations by

250 Dorfman and others may be explained by the distortion of coordination polyhedron as
251 argued for an Fe^{3+}-rich sodium silicate glass (Prescher et al., 2014).

252 **3.3. Disproportionation of Fe^{2+} in a Deep Magma Ocean**

253 The earlier experiments performed by Armstrong et al. (2019) observed that the $Fe^{3+}/\Sigma Fe$
254 ratio in a silicate melt increased with increasing pressure above 10 GPa under a given
255 oxygen fugacity buffer, suggesting that Fe^{2+} disproportionates into Fe^{3+} and metal in a
256 deep magma ocean. They attributed it to the smaller partial molar volume of $FeO_{1.5}$ than
257 that of FeO in melt above 10 GPa. Indeed, the present study indicates that the coordination
258 number of Fe^{3+} increases rapidly from four at 1 atm to six at ~15 GPa (Figure 2). It causes
259 a remarkable reduction in the partial molar volume V of $FeO_{1.5}$ compared to that of FeO
260 in this pressure range. These support negative ΔV (= $V_{FeO1.5}$ - V_{FeO}) and resulting the
261 disproportionation of Fe^{2+} in the magma ocean above 10 GPa (Armstrong et al., 2019).
262 The recent first principles study by Deng et al. (2020) reported the positive ΔV even above
263 10 GPa, but it is likely due to an underestimation of the coordination number of Fe^{2+} at
264 ambient pressure, which leads to an overestimation of the compressibility of the partial
265 molar volume of FeO.

266 With increasing pressure above ~15 GPa, the Fe^{2+}-O bond length changed similarly to
267 that of Fe^{3+}-O (Figure 4c). This means that ΔV is almost unchanged upon compression in
268 this pressure range, at least to 60 GPa. If ΔV is negative at 10–25 GPa (Armstrong et al.,
269 2019), it stays negative and expands the stability of Fe^{3+} relative to Fe^{2+} in silicate melts
270 at higher pressures. It therefore supports that the disproportionation of FeO into $Fe_{1.5}O$
271 and metal Fe in a magma ocean is more enhanced with increasing pressure above 10 GPa
272 to lower-mantle conditions. Metal Fe produced by such disproportionation reaction may

have been segregated into the Earth's core, increasing the oxygen fugacity of the magma ocean, which changed the metal-silicate partitioning of siderophile elements (Wade & Wood, 2005) and the composition of early Earth atmosphere (Hirschmann, 2012).

4. Conclusions

Present *in-situ* high-pressure XAFS measurements elucidated the compression behavior of the coordination environments around Fe^{2+} and Fe^{3+} in basaltic glasses up to 83 GPa and 60 GPa, respectively. Pre-edge and EXAFS analyses demonstrated that between 1 atm and ~15 GPa, the coordination number of Fe^{2+} increased from ~5 to 6, while that of Fe^{3+} augmented from almost 4 to 6. At higher pressures, both Fe^{2+}-O and Fe^{3+}-O bond lengths decreased smoothly with increasing pressure, indicating minimal increase in their coordination number. In this pressure range, the observed compression behaviors of the Fe^{2+}-O and Fe^{3+}-O bonds are similar to those of earlier theoretical predictions of high-spin Fe^{2+} and Fe^{3+} in $Mg_{0.75}Fe^{2+}_{0.25}SiO_3$ and $Mg_{0.875}Fe^{3+}_{0.25}Si_{0.875}O_3$ melts, respectively, suggesting both Fe^{2+} and Fe^{3+} in the basaltic glasses remain high-spin at least to the maximum pressures explored here.

A larger change in the coordination number of Fe^{3+} than that of Fe^{2+} below 15 GPa suggests that the partial molar volume of $FeO_{1.5}$ is more compressible than that of FeO in this pressure range. It will lead to negative ΔV (= $V_{FeO1.5}$ - V_{FeO}) above 10 GPa (Armstrong et al., 2019), which drives the disproportionation of Fe^{2+} into Fe^{3+} and metal Fe in a deep magma ocean. Our data showed that the both the Fe^{2+}-O and Fe^{3+}-O bond lengths decreased similarly with increasing pressure above 15 GPa. It suggests that ΔV would remain negative upon compression at least to 60 GPa, which accelerates the disproportionation reaction at deeper level of the magma ocean.

Open Research

Datasets for this research are found in Tables S1 and S2 available online (from https://doi.org/10.5281/zenodo.5749615).

Acknowledgments

K. Yonemitsu is acknowledged for her help in EPMA analyses. This work was supported by the JSPS grants 21H04968 and 20J21667. XAFS measurements was performed with the approval of the Photon Factory (proposal no. 2018S1-001 and 2020G670).

References

Alderman, O. L. G., Wilding, M. C., Tamalonis, A., Sendelbach, S., Heald, S. M., Benmore, C. J., Johnson, C. E., Johnson, J. A., Hah, H.-Y., & Weber, J. K. R. (2017). Iron K-edge X-ray absorption near-edge structure spectroscopy of aerodynamically levitated silicate melts and glasses. *Chemical Geology*, *453*, 169–185. https://doi.org/10.1016/j.chemgeo.2017.01.020

Armstrong, K., Frost, D. J., McCammon, C. A., Rubie, D. C., & Ballaran, T. B. (2019). Deep magma ocean formation set the oxidation state of Earth's mantle. *Science*, *365*, 903–906. https://doi.org/10.1126/science.aax8376

Badro, J., Fiquet, G., Guyot, F., Rueff, J. P., Struzhkin, V. V., Vankó, G., & Monaco, G. (2003). Iron partitioning in Earth's mantle: toward a deep lower mantle discontinuity. *Science*, *300*, 789–791. https://doi.org/10.1126/science.1081311

Bajgain, S., Ghosh, D. B., & Karki, B. B. (2015). Structure and density of basaltic melts at mantle conditions from first-principles simulations. *Nature communications*, *6*, 8578. https://doi.org/10.1038/ncomms9578

Berry, A. J., O'Neill, H. S. C., Jayasuriya, K. D., Campbell, S. J., & Foran, G. J. (2003). XANES calibrations for the oxidation state of iron in a silicate glass. *American Mineralogist*, *88*, 967–977. https://doi.org/10.2138/am-2003-0704

Boubnov, A., Lichtenberg, H., Mangold, S., & Grunwaldt, J. D. (2015). Identification of the iron oxidation state and coordination geometry in iron oxide-and zeolite-based catalysts using pre-edge XAS analysis. *Journal of Synchrotron Radiation*, *22*, 410–426. https://doi.org/10.1107/S1600577514025880

Deng, J., Du, Z., Karki, B. B., Ghosh, D. B., & Lee, K. K. (2020). A magma ocean origin to divergent redox evolutions of rocky planetary bodies and early atmospheres. *Nature communications*, *11*, 2007. https://doi.org/10.1038/s41467-020-15757-0

Dorfman, S. M., Dutton, S. E., Potapkin, V., Chumakov, A. I., Rueff, J. P., Chow, P., Xiao, Y., Cava, R. J., Duffy, T. S., McCammon, C. A., & Gillet, P. (2016). Electronic transitions of iron in almandine-composition glass to 91 GPa. *American Mineralogist*, *101*, 1659–1667. https://doi.org/10.2138/am-2016-5606

Farges, F., Lefrère, Y., Rossano, S., Berthereau, A., Calas, G., & Brown Jr, G. E. (2004). The effect of redox state on the local structural environment of iron in silicate glasses: A combined XAFS spectroscopy, molecular dynamics, and bond valence study. *Journal of Non-Crystalline Solids*, *344*, 176–188. https://doi.org/10.1016/j.jnoncrysol.2004.07.050

Ghosh, D. B., & Karki, B. B. (2018). First-principles molecular dynamics simulations of anorthite ($CaAl_2Si_2O_8$) glass at high pressure. *Physics and Chemistry of Minerals*, *45*, 575–587. https://doi.org/10.1007/s00269-018-0943-4

Ghosh, D. B., & Karki, B. B. (2020). Effects of valence and spin of Fe in $MgSiO_3$ melts: structural insights from first-principles molecular dynamics simulations. *Geochimica et Cosmochimica Acta*, *279*, 107–118. https://doi.org/10.1016/j.gca.2020.03.040

Giuli, G., Alonso-Mori, R., Cicconi, M. R., Paris, E., Glatzel, P., Eeckhout, S. G., & Scaillet, B. (2012). Effect of alkalis on the Fe oxidation state and local environment in peralkaline rhyolitic glasses. *American Mineralogist*, *97*, 468–475. https://doi.org/10.2138/am.2012.3888

Gu, C., Catalli, K., Grocholski, B., Gao, L., Alp, E., Chow, P., Xiao, Y., Cynn, H., Evans, W. J., & Shim, S. H. (2012). Electronic structure of iron in magnesium silicate glasses at high pressure. *Geophysical Research Letters*, *39*. https://doi.org/10.1029/2012GL053950

Hirschmann, M. M. (2012). Magma ocean influence on early atmosphere mass and composition. *Earth and Planetary Science Letters*, *341–344*, 48–57. https://doi.org/10.1016/j.epsl.2012.06.015

Hong, X., Newville, M., Duffy, T. S., Sutton, S. R., & Rivers, M. L. (2014). X-ray absorption spectroscopy of GeO_2 glass to 64 GPa. *Journal of Physics: Condensed Matter*, *26*, 035104. https://doi.org/10.1088/0953-8984/26/3/035104

Karki, B. B., Ghosh, D. B., Maharjan, C., Karato, S. I., & Park, J. (2018). Density-pressure profiles of Fe-bearing $MgSiO_3$ liquid: effects of valence and spin states, and implications for the chemical evolution of the lower mantle. *Geophysical Research Letters*, *45*, 3959–3966. https://doi.org/10.1029/2018GL077149

Kress, V. C., & Carmichael, I. S. E. (1991). The compressibility of silicate liquids containing Fe_2O_3 and the effect of composition, temperature, oxygen fugacity and

363 pressure on their redox states. *Contributions to Mineralogy and Petrology*, *108*, 82–
364 92. https://doi.org/10.1007/BF00307328
365 Lange, R. A., & Carmichael, I. S. E. (1987). Densities of Na_2O-K_2O-CaO-MgO-FeO-
366 Fe_2O_3-Al_2O_3-TiO_2-SiO_2 liquids: new measurements and derived partial molar
367 properties. *Geochimica et Cosmochimica Acta*, *51*, 2931–2946.
368 https://doi.org/10.1016/0016-7037(87)90368-1
369 Mao, Z., Lin, J. F., Yang, J., Wu, J., Watson, H. C., Xiao, Y., Chow, P., & Zhao, J. (2014).
370 Spin and valence states of iron in Al-bearing silicate glass at high pressures studied
371 by synchrotron Mössbauer and X-ray emission spectroscopy. *American Mineralogist*,
372 *99*, 415–423. https://doi.org/10.2138/am.2014.4490
373 Murakami, M., Goncharov, A. F., Hirao, N., Masuda, R., Mitsui, T., Thomas, S. M., &
374 Bina, C. R. (2014). High-pressure radiative conductivity of dense silicate glasses with
375 potential implications for dark magmas. *Nature communications*, *5*, 5428.
376 https://doi.org/10.1038/ncomms6428
377 Nomura, R., Ozawa, H., Tateno, S., Hirose, K., Hernlund, J., Muto, S., Ishii, H., &
378 Hiraoka, N. (2011). Spin crossover and iron-rich silicate melt in the Earth's deep
379 mantle. *Nature*, *473*, 199–202. https://doi.org/10.1038/nature09940
380 O'Neill, H. S. C., Berry, A. J., McCammon, C. C., Jayasuriya, K. D., Campbell, S. J., &
381 Foran, G. (2006). An experimental determination of the effect of pressure on the
382 $Fe^{3+}/\Sigma Fe$ ratio of an anhydrous silicate melt to 3.0 GPa. *American Mineralogist*, *91*,
383 404–412. https://doi.org/10.2138/am.2005.1929
384 Ozawa, K., Hirose, K., Kuwayama, Y., & Takahashi, Y. (2021). The pressure-induced
385 local structural change around tungsten in silicate glass. *Geochemical Perspectives*
386 *Letters*, *18*. https://doi.org/10.7185/geochemlet.2116

Prescher, C., Weigel, C., McCammon, C., Narygina, O., Potapkin, V., Kupenko, I., Sinmyo, R., Chumakov, A. I., & Dubrovinsky, L. (2014). Iron spin state in silicate glass at high pressure: implications for melts in the Earth's lower mantle. *Earth and Planetary Science Letters*, *385*, 130–136. https://doi.org/10.1016/j.epsl.2013.10.040

Prescher, C., Prakapenka, V. B., Stefanski, J., Jahn, S., Skinner, L. B., & Wang, Y. (2017). Beyond sixfold coordinated Si in SiO_2 glass at ultrahigh pressures. *Proceedings of the National Academy of Sciences USA*, *114*, 10041–10046. https://doi.org/10.1073/pnas.1708882114

Sanloup, C., Drewitt, J., Konôpková, Z., Dalladay-Simpson, P., Morton, D. M., Rai, N., Van Westrenen, W., & Morgenroth, W. (2013a). Structural change in molten basalt at deep mantle conditions. *Nature*, *503*, 104–107. https://doi.org/10.1038/nature12668

Sanloup, C., Drewitt, J. W. E., Crépisson, C., Kono, Y., Park, C., McCammon, C., Hennet, L., Brassamin, S., & Bytchkov, A. (2013b). Structure and density of molten fayalite at high pressure. *Geochimica et Cosmochimica Acta*, *118*, 118–128. https://doi.org/10.1016/j.gca.2013.05.012

Solomatova, N. V., Jackson, J. M., Sturhahn, W., Rossman, G. R., & Roskosz, M. (2017). Electronic environments of ferrous iron in rhyolitic and basaltic glasses at high pressure. *Journal of Geophysical Research: Solid Earth*, *122*, 6306–6322. https://doi.org/10.1002/2017JB014363

Solomatova, N. V., & Caracas, R. (2019). Pressure-induced coordination changes in a pyrolitic silicate melt from ab initio molecular dynamics simulations. *Journal of Geophysical Research: Solid Earth*, *124*, 11232–11250. https://doi.org/10.1029/2019JB018238

411 Spiekermann, G., Harder, M., Gilmore, K., Zalden, P., Sahle, C. J., Petitgirard, S., Wilke,
412 M., Biedermann, N., Weis, C., Morgenroth, W., Tse, J. S., Kulik, E., Nishiyama, N.,
413 Yavas, H., & Sternemann, C. (2019). Persistent octahedral coordination in
414 Amorphous GeO_2 up to 100 GPa by K β″ X-Ray emission spectroscopy. *Physical*
415 *Review X*, *9*, 011025. https://doi.org/10.1103/PhysRevX.9.011025
416 Wade, J., & Wood, B. J. (2005). Core formation and the oxidation state of the Earth.
417 *Earth and Planetary Science Letters*, *236*, 78–95.
418 https://doi.org/10.1016/j.epsl.2005.05.017
419 Waychunas, G. A., Apted, M. J., & Brown Jr., G. E. (1983). X-ray K-edge absorption
420 spectra of Fe minerals and model compounds: near-edge structure. *Physics and*
421 *Chemistry of Minerals*, *10*, 1–9. https://doi.org/10.1007/BF01204319
422 Wilke, M., Farges, F., Petit, P. E., Brown Jr., G. E., & Martin, F. (2001). Oxidation state
423 and coordination of Fe in minerals: an Fe K-XANES spectroscopic study. *American*
424 *Mineralogist*, *86*, 714–730. https://doi.org/10.2138/am-2001-5-612
425 Wilke, M., Partzsch, G. M., Bernhardt, R., & Lattard, D. (2005). Determination of the
426 iron oxidation state in basaltic glasses using XANES at the K-edge. *Chemical*
427 *Geology*, *220*, 143–161. https://doi.org/10.1016/j.chemgeo.2005.03.004
428 Wilke, M., Farges, F., Partzsch, G. M., Schmidt, C., & Behrens, H. (2007). Speciation of
429 Fe in silicate glasses and melts by in-situ XANES spectroscopy. *American*
430 *Mineralogist*, *92*, 44–56. https://doi.org/10.2138/am.2007.1976
431 Zhang, F., & Oganov, A. R. (2006). Valence state and spin transitions of iron in Earth's
432 mantle silicates. *Earth and Planetary Science Letters*, *249*, 436–443.
433 https://doi.org/10.1016/j.epsl.2006.07.023

Zhang, H. L., Hirschmann, M. M., Cottrell, E., & Withers, A. C. (2017). Effect of pressure on $Fe^{3+}/\Sigma Fe$ ratio in a mafic magma and consequences for magma ocean redox gradients. *Geochimica et Cosmochimica Acta*, *204*, 83–103. https://doi.org/10.1016/j.gca.2017.01.023

References from the supporting information

Akahama, Y., & Kawamura, H. (2004). High-pressure Raman spectroscopy of diamond anvils to 250 GPa: Method for pressure determination in the multimegabar pressure range. *Journal of Applied Physics*, *96*, 3748–3751. https://doi.org/10.1063/1.1778482

Berry, A. J., Stewart, G. A., O'Neill, H. S. C., Mallmann, G., & Mosselmans, J. F. W. (2018). A re-assessment of the oxidation state of iron in MORB glasses. *Earth and Planetary Science Letters*, *483*, 114–123. https://doi.org/10.1016/j.epsl.2017.11.032

Mao, H. K., Bell, P. M., Shaner, J. T., & Steinberg, D. J. (1978). Specific volume measurements of Cu, Mo, Pd, and Ag and calibration of the ruby R_1 fluorescence pressure gauge from 0.06 to 1 Mbar. *Journal of Applied Physics*, *49*, 3276–3283. https://doi.org/10.1063/1.325277

Merkel, S., & Yagi, T. (2005). X-ray transparent gasket for diamond anvil cell high pressure experiments. *Review of Scientific Instruments*, *76*, 046109. https://doi.org/10.1063/1.1884195

Zabinsky, S. I., Rehr, J. J., Ankudinov, A., Albers, R. C., & Eller, M. J. (1995). Multiple-scattering calculations of X-ray-absorption spectra. *Physical Review B*, *52*, 2995. https://doi.org/10.1103/PhysRevB.52.2995

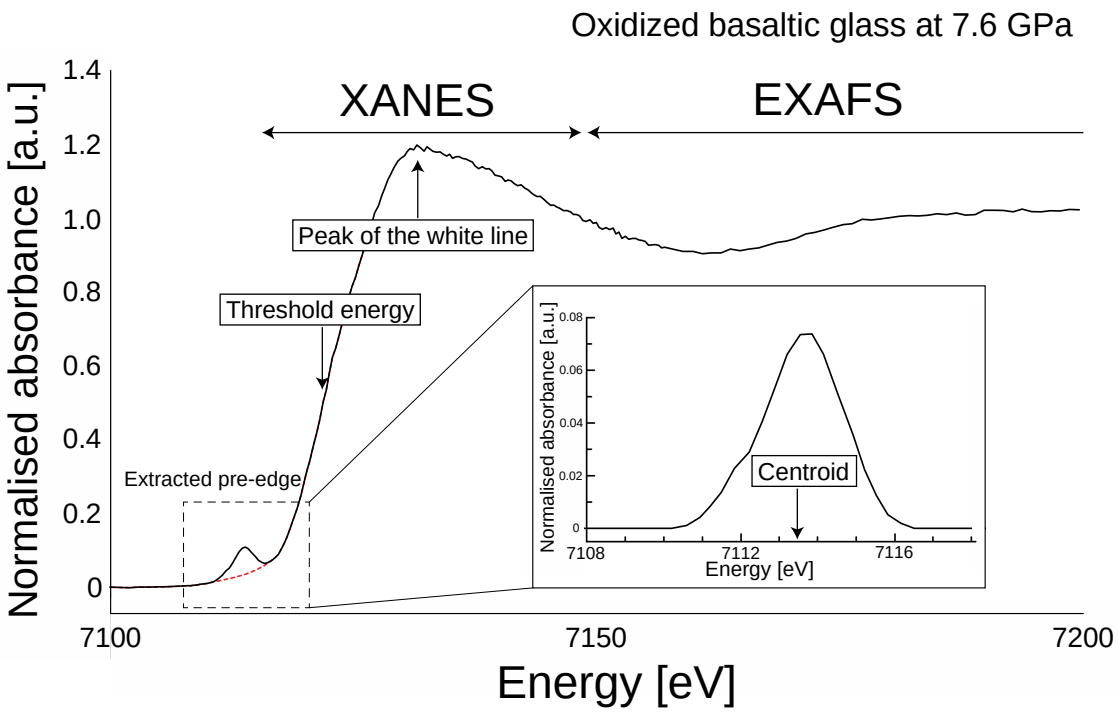

Figure 1. The μ-XAFS spectrum of oxidized basaltic glass in a DAC collected at 7.6 GPa, including the pre-edge features with centroid position, XANES with the threshold energy and the peak of the while line, and EXAFS oscillations. Red dashed line is a cubic spline function for the background of the pre-edge signals (Wilke et al., 2001).

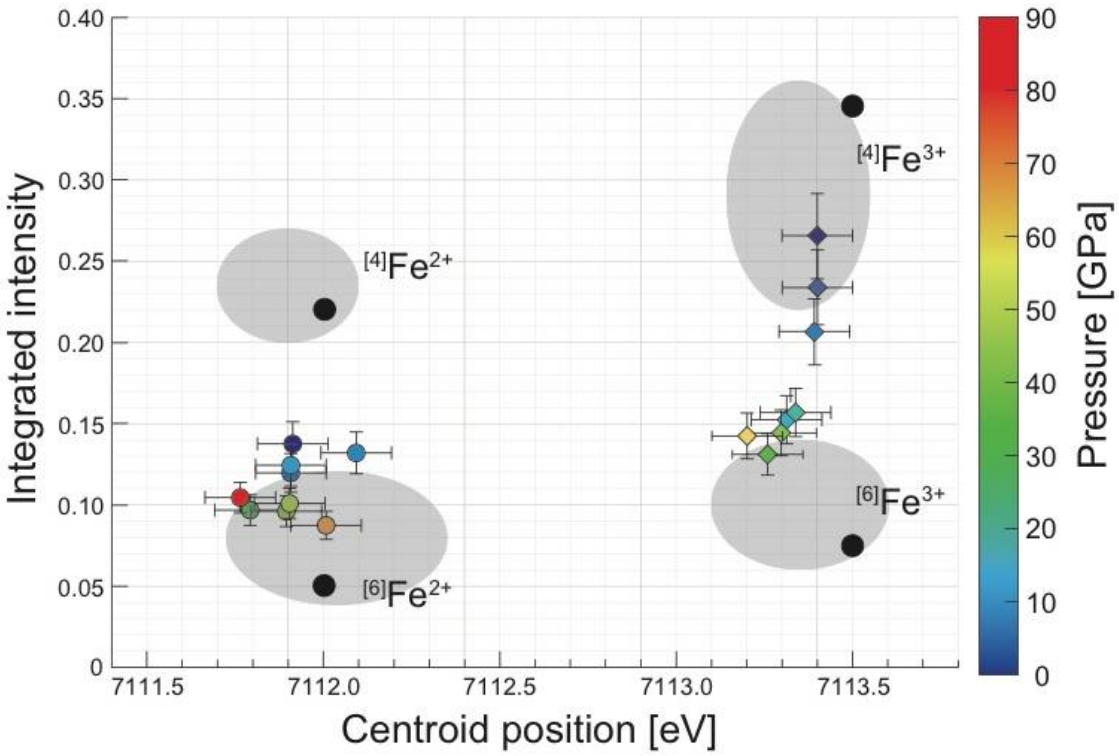

Figure 2. The pre-edge variogram of the centroid position vs. integrated intensity for reduced (circles) and oxidized basaltic glasses (diamonds) at high pressures. Pressure is given by color. Shaded areas indicate the ranges for ferrous and ferric iron with four- and six-fold coordination (Boubnov et al., 2015). Black circles represent the data for minerals with 4- and 6-fold ferrous/ferric iron given by Wilke et al. (2001).

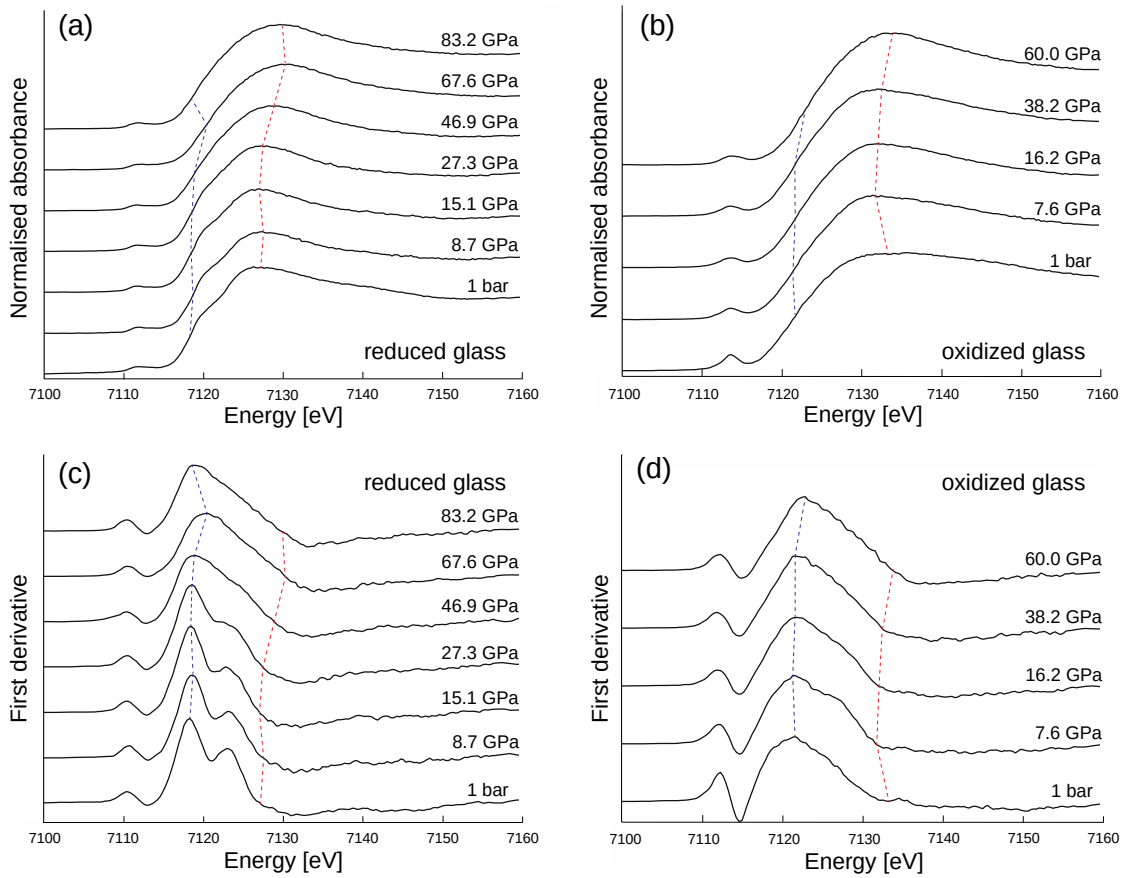

Figure 3. Fe K-edge XANES spectra and their first derivative spectra obtained by three-point moving average for reduced (a, c) and oxidized (b, d) basaltic glasses at high pressures. The spectrum of the reduced glass at 67.6 GPa is of a W-doped basaltic glass used in Ozawa et al. (2021). Red and blue dashed lines indicate pressure-evolutions of the peak energy of the white line and the threshold energy, respectively (see Figure 1).

F

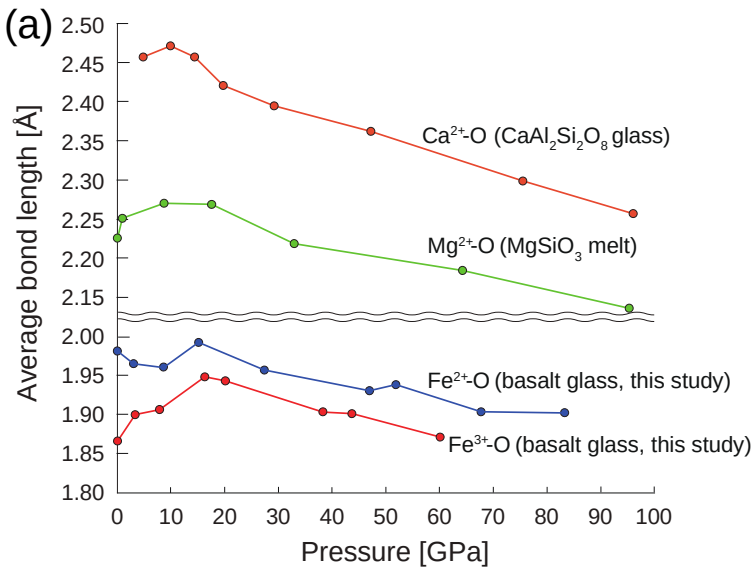
(a)
Average bond length [Å]
Pressure [GPa]
Ca2+-O (CaAl2Si2O8 glass)
Mg2+-O (MgSiO3 melt)
Fe2+-O (basalt glass, this study)
Fe3+-O (basalt glass, this study)

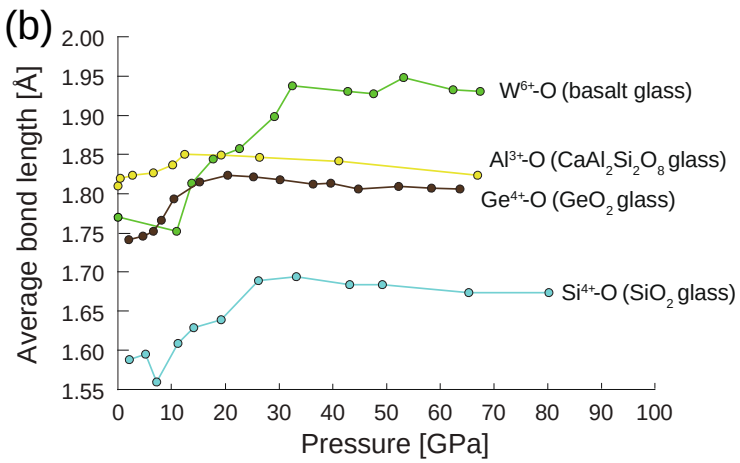
(b)
Average bond length [Å]
Pressure [GPa]
W6+-O (basalt glass)
Al3+-O (CaAl2Si2O8 glass)
Ge4+-O (GeO2 glass)
Si4+-O (SiO2 glass)

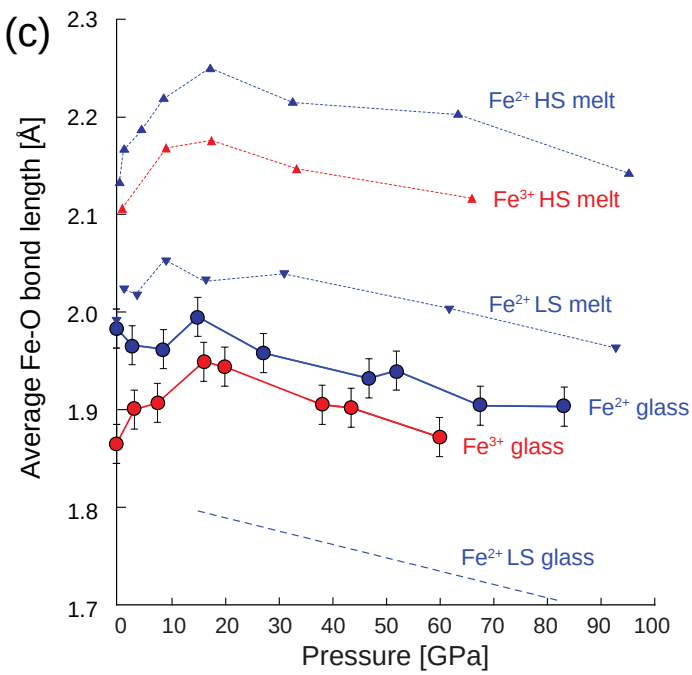
(c)
Average Fe-O bond length [Å]
Pressure [GPa]
Fe2+ HS melt
Fe3+ HS melt
Fe2+ LS melt
Fe2+ glass
Fe3+ glass
Fe2+ LS glass

478

Figure 4. (a, b) Interatomic distances between various cations and oxygen in silicate/germanate melt and glasses; Ca^{2+}-O and Al^{3+}-O (Ghosh & Karki, 2018), Mg^{2+}-O (Ghosh & Karki, 2020), $Fe^{2+/3+}$-O (this study), Si^{4+}-O (Prescher et al., 2017), Ge^{4+}-O (Hong et al., 2014), and W^{6+}-O (Ozawa et al., 2021). (c) Comparison of the Fe^{2+}-O (blue lines) and Fe^{3+}-O (red lines) bond lengths in our basaltic glasses with those in Fe-bearing $MgSiO_3$ melts (dotted lines) at 3000 K obtained by ab initio molecular dynamics simulations (Ghosh & Karki, 2020). The blue dashed line is for low-spin Fe^{2+} in the glass, estimated from a difference in the calculated Fe^{2+}-O bond length between high-spin and low-spin states.